Enhanced methane conversion in chemical looping partial oxidation systems using a copper doping modification

Lang Qin[a,1,2], Mengqing Guo[a,1,2], Yan Liu[a,1,2], Zhuo Cheng[a,1,2], Jonathan A. Fan[b], Liang-Shih Fan[a,*]

[a] *William G. Lowrie Department of Chemical and Biomolecular Engineering, The Ohio State University, 151 W. Woodruff Ave, Columbus, OH, 43210, USA*
[b] *Department of Electrical Engineering, Ginzton Laboratory, Spilker Engineering and Applied Sciences, Stanford University, 348 Via Pueblo Mall, Stanford, CA, 94305, USA*

A B S T R A C T

Chemical looping partial oxidation (CLPO) is a promising strategy of methane conversion to syngas with low cost and minimal environmental impact. A major challenge is the development of oxygen carriers that have high reactivity, high oxygen carrying capacity, and recyclability. We demonstrate that the addition of a low concentration (1%) of copper dopant to iron-based oxygen carriers can dramatically enhance the reactivity in CLPO process at low temperatures while maintaining the recyclability of these carriers. With the dopant, the methane conversion rate at 700 °C is 470% higher than that of carriers without the dopant. These results are substantiated by *ab initio* DFT + U and thermochemistry analyses. It is noted that operating a chemical looping system at 700 °C can result in energy consumption savings of ~35% as compared to a chemical looping operation at 1000 °C. Thus, our findings provide a pathway to significantly lowering the methane reaction temperature in chemical looping systems, which will lead to substantial energy savings with desired oxygen carrier recyclability.

1. Introduction

Biomass-generated methane is a renewable and sustainable energy source for the synthesis of syngas and value-added chemicals. It is a topic of immense academic and industrial interest because it is now economically and commercially viable to obtain biomass-generated methane with a quality similar to fossil natural gas. To reduce the material and energy cost of the methane-to-syngas conversion process, it is imperative to identify strategies in methane-to-syngas generation that operate efficiently at low temperatures [1]. Energy savings are particularly important in industry due to its considerable environmental and economic impact. From a process point of view, lowering the temperature of operation will decelerate materials obliteration in harsh reactors.

Methane-to-syngas generation is traditionally achieved using autothermal reforming or dry (CO_2) reforming. The reforming reactions are highly endothermic and require operating temperatures of 900 °C or above to attain high conversion rate and to minimize the thermodynamic driving force for carbon deposition. To reduce these operating temperatures while counteracting carbon deposition, noble metals, such as Pt, Pd and Au are often added to the metal oxide materials as catalytic dopants. However, the addition of noble metals makes these processes costly [2].

An alternative approach to methane-to-syngas generation is the chemical looping process, which is one of the most promising techniques in the clean energy industry. It is highly efficient for methane conversion without any energy penalty, as required generally by other syngas purification processes. The core of chemical looping technology depends on complex redox reactions involving hydrocarbon molecules absorption and dissociation on metal-oxide based oxygen carrier surfaces, lattice oxygen ion diffusion, oxygen vacancy creation and annihilation at high temperatures, as illustrated in Fig. 1. The cycles of chemical looping partial oxidation (CLPO) process allows continuous generation of high purity syngas with a controllable CO to H_2 ratio and a near-zero CO_2 emission.

Enormous efforts have been spent in the past two decades to improve oxygen carrier reactivity at lower temperatures [2–10]. Pt- or Rh-promoted CeO_2 with a γ-Al_2O_3 support [1] can lower the reaction
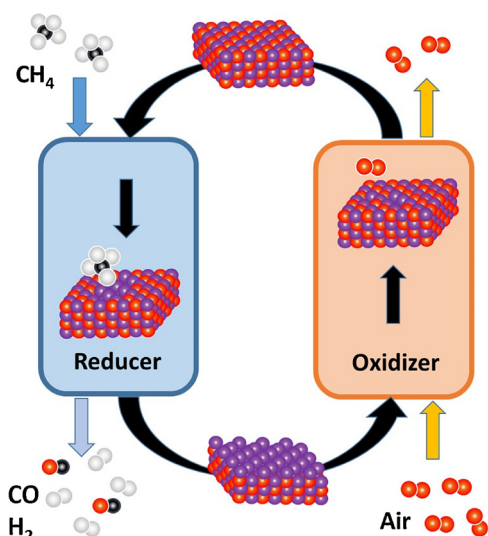

Fig. 1. Concept of chemical looping partial oxidation with methane.

temperatures induced by the promoters, but at the expense of severe carbon deposition. The modification of ceria with transition metals for the purposes of improving oxygen carrier reactivity has also been investigated [4–7]. However, the addition of Mn in CeO_2 oxygen carriers results in a tendency of complete methane oxidation, whereas CO and H_2O were found to be the main production in Nb-modified CeO_2. Modifications to perovskite materials have also been investigated [8,9], which can increase the capacity of the oxygen carriers, but reduce their

selectivity to syngas and particle reactivity with CH_4 [10].

To date, iron-based oxygen carriers have been demonstrated as the most promising material system for commercially viable oxygen carrier particles in chemical looping techniques including CLPO [11]. To further improve carrier performance, a general strategy is to incorporate low concentrations of isovalent non-noble metal dopant into the carrier, which can modify its chemical properties without dramatically increasing cost or impacting its phase integrity and high oxygen carrying capacity [12,13]. Isovalent dopants, such as rare earth elements, can provide surface catalytic sites to decrease methane partial oxidation activation energy, thereby improving oxygen carrier reactivity [12]. Nevertheless, due to the fact that isovalent dopants such as La create little Schottky defects, the impact of oxygen vacancy in the isovalent-dopant modified samples is small. It remains highly challenging to find a dopant that can not only facilitate the formation of oxygen vacancies that promote ion transport, but also reduce methane partial oxidation activation energy and even alter the reaction mechanism with a more favorable reaction pathway for methane partial oxidation.

In this work, we report that the aliovalent dopant Cu can universally increase methane conversion rates without losing high oxygen carrying capacity or phase integrity at reaction temperatures as low as 700 °C and overall, 1% Cu-dopant concentration has the best reactivity improvement with lowest cost increase without decreasing oxygen carrying capacity or mechanical strength of iron oxides. Our simulation work indicates that the Cu dopants not only provide active sites on metal oxide surface, but also create oxygen vacancies which will promote ionic diffusion and also further lower methane activation energy.
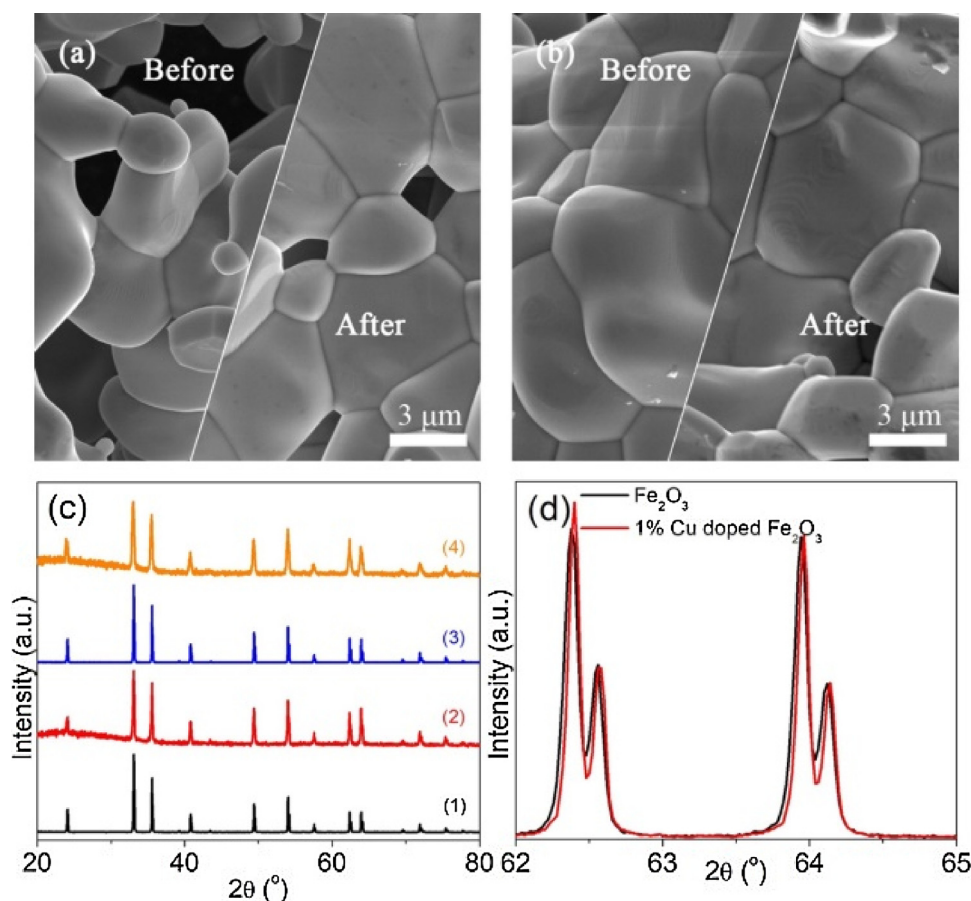

Fig. 2. SEM images of (a) Fe_2O_3 and (b) 1% Cu-doped Fe_2O_3 samples before and after redox reaction. (c) XRD patterns of Fe_2O_3 (1) before and (2) after 45 cyclic redox reaction compared with 1% Cu-doped Fe_2O_3 (3) before and (4) after 45 cyclic redox reaction. (d) small range XRD pattern of Fe_2O_3 and 1% Cu-doped Fe_2O_3.

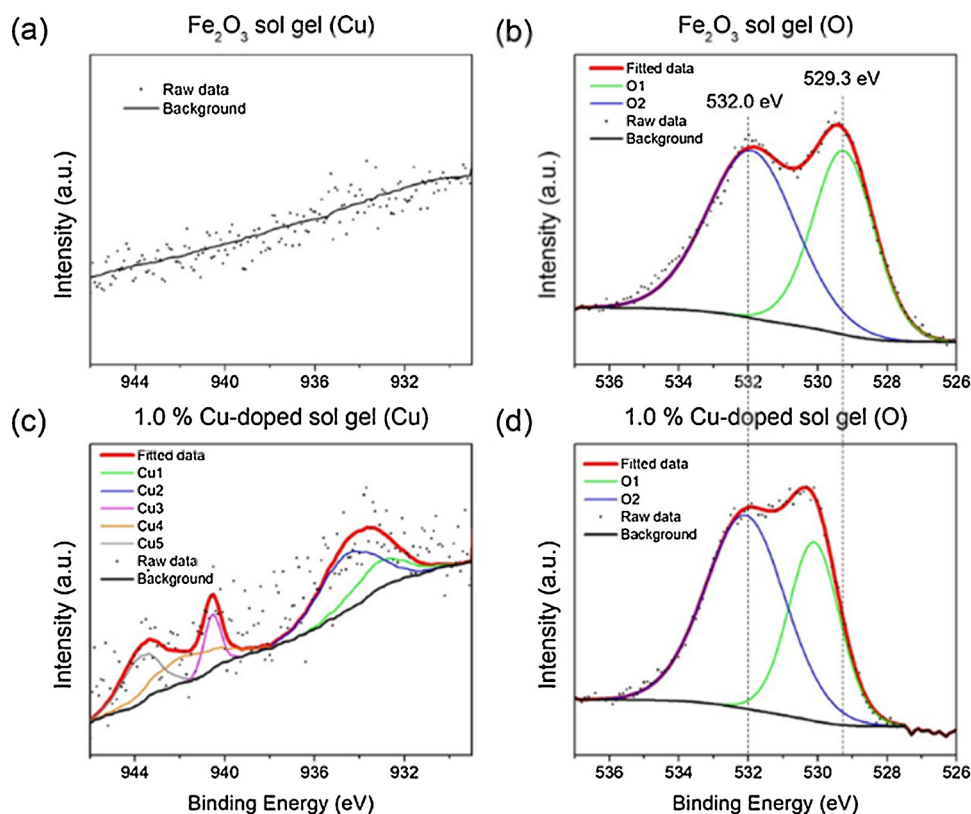**Fig. 3.** XPS Cu 2p3/2 spectra of (a) undoped Fe_2O_3 (c) 1% Cu-doped Fe_2O_3; O 1 s spectra of (b) undoped Fe_2O_3 (d) 1% Cu-doped Fe_2O_3.

Table 1
The distribution of different Cu or O species in samples.

Sample	O 1s lattice oxide	O 1s hydrated or defective oxide	Cu/O (%)
Fe_2O_3	43.1	56.9	0
1% Cu-doped Fe_2O_3	37.2	62.8	0.89

2. Experimental

2.1. Sample preparation

1% Cu doped Fe_2O_3 as well as non doped Fe_2O_3 were made by the sol gel method. The sol gel solutions were prepared by dissolving Fe $(NO_3)_3 \cdot 9H_2O$ (Acros Organics, 99 + %, for analysis) with Cu $(NO_3)_2 \cdot 3H_2O$ (Acros Organics, 99 + %, for analysis) stoichiometrically in 1 mol/L HNO_3 (Fisher Scientific, 1.0 N) solution, followed by the addition of citric acid anhydrous (Fisher Scientific, 100.0% assay). The pH value of the aforementioned solutions were adjusted to ~7.3 by NH_4OH (Fisher Scientific, 28–30%) solution. The whole solution was mixed with ethanol under vigorous stirring. The eventual molar ratio of nitrate salt: citric acid: ethanol was 1:2:2. The solution was concentrated by heating at 270 °C for 1.5 h by hot plate and otherwise ambient conditions. Thus, the obtained precursors were heated in the furnace with ambient air at 600 °C for 3 h to remove organic residues by 1 °C/min heating ramp rate and 6 °C/min cooling ramp rate. Afterwards, this was followed by calcination at 1100 °C for 2 h using 2 °C/min heating ramp rate and 6 °C/min cooling ramp rates. Finally, the samples were moved to a small crucible to calcinate at 1260 °C for 4 h by 2 °C/min both heating and cooling ramp rates.

2.2. TGA test

The as prepared samples with approximately 15 mg were mounted

in an alumina crucible, and continuous 15 reduction-oxidation cycles were conducted at four different temperatures from 1000 °C to 700 °C using a Setaram SETSYS Evolution Thermogravimetric Analyzer (TGA). The reduction step was performed using 25% CH_4 (50 mL/min) balanced by inert gas (50 ml/min N_2 and 100 ml/min Helium as the carrier gas) for 5 min. The oxidation step was performed by 25% air (50 mL/min) balanced with inert gas (50 ml/min N_2 and 100 ml/min Helium as the carrier gas) for 5 min. Meanwhile, there is a 10 min flushing step using the same flow rate of inert gas to prohibit the mixing of oxygen and CH_4. Before reduction-oxidation cycles, these powders were treated at 800 °C for 5 reduction-oxidation cycles to activate their reactivity. When analyzing the TGA data, reduction conversion is defined by the following equation:

$$Xr = \frac{wi - wt}{wo} \times 100\%$$

where *wi* is the initial weight (mg) of oxygen carriers in TGA, *wt* is the weight of oxygen carriers after 5 min reduction of materials by 25% CH_4, and *wo* represents the weight of oxygen in initial oxygen carriers. The definition of oxidation conversion is shown as the following equation:

$$Xr = \frac{wf - wt}{wo} \times 100\%$$

where **wf** is the final weight of oxygen carriers after oxidation regeneration, **wt** is the weight of oxygen carriers before oxidation regeneration, and **wo** represents the weight of oxygen in initial oxygen carriers.

2.3. Phase characterization

These samples were also analyzed using a Rigaku SmartLab X-ray Diffractometer (XRD) with eliminated fluorescence. Scans were run from 20 to 80 degrees at a rate of 1° per minute with an accelerating
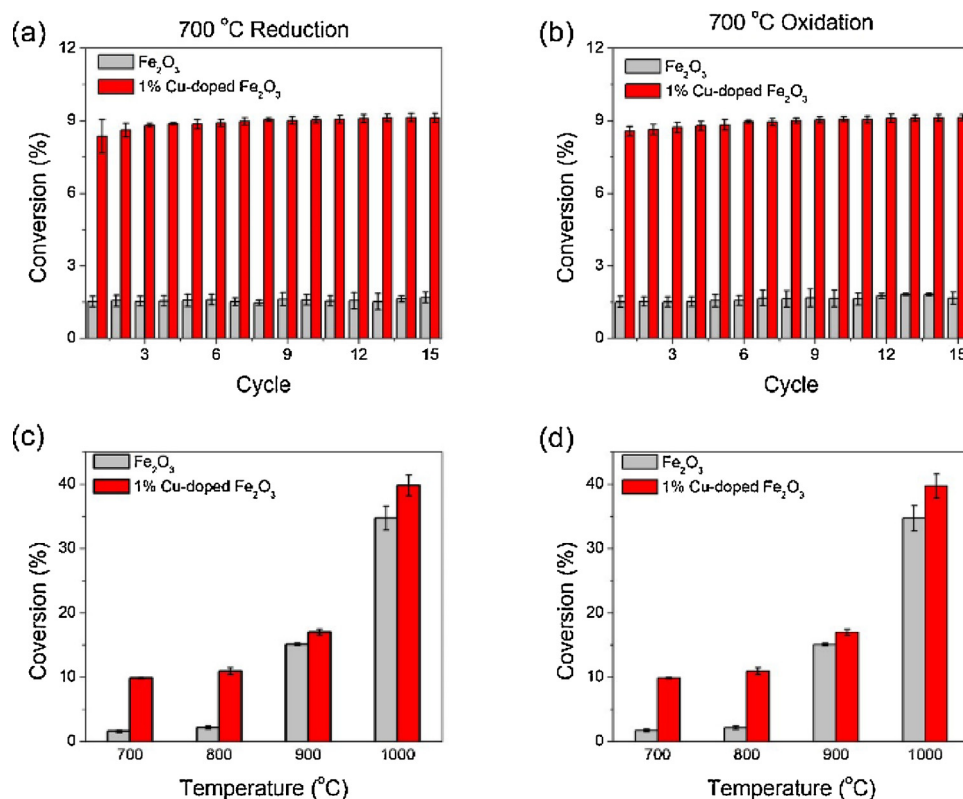
Fig. 4. Cyclic oxygen carrier conversion rates of undoped Fe_2O_3 and 1% Cu doped iron oxide at 700 °C with 25% CH_4 balanced by inert gas of (a) reduction and (b) oxidation; Average oxygen carrier conversion rates of undoped Fe_2O_3 and 1% Cu doped iron oxide at different temperatures (c) reduction and (d) oxidation.

voltage and filament current of 40 kV and 44 mA, respectively. The small range scan of XRD was run from 62 to 65 degrees with a rate of 0.1 °/minute with the same set up of voltage and filament current. All of the XRD spectra were analyzed using PDXL software and identified with the JCPDS database. Scanning electron microscope (SEM) images were examined with a 10 kV and 0.17 nA electron beam. Secondary electron images were obtained with a working distance of 4.1 mm. A Kratos Axis Ultra DLD spectrometer was used to obtain X-ray photoelectron (XPS) spectra. Mg Kα monochromatic X-ray radiation (1253.8 eV) was applied to ensure the optimal peak intensity of Cu. The spectra were collected at room temperature. Binding energy (B.E.) values were referenced to the standard C 1 s binding energy of 284.8 eV. The CasaXPS program was used for data analysis. Shirley-type background and Lorentzian-Gaussian combination were used for data processing.

2.4. DFT calculations

The first-principle calculations were performed within the framework of density functional theory (DFT), using the Vienna Ab Initio Simulation Package (VASP) [14–16]. The generalized gradient approximation of Perdew, Burke and Ernzerhof [17] used to represent the exchange-correlation energy. The projector-augmented wave (PAW) method, with a 400 eV energy cutoff, was used to describe the wave functions of the atomic cores. The tetrahedron method with Blöchl corrections was used to set the partial occupancies for the orbitals. While several k-point mesh sizes (e.g.,$4 \times 4 \times 1$ up to $13 \times 13 \times 1$) were considered, ultimately the $8 \times 8 \times 1$ Monkhorst-Pack k-point mesh was used for surface calculations to give results that were converged within $1 \times 10 - 5$ eV, using the conjugate gradient method. To study the effect of incorporating Cu, a single Fe atom was replaced by a Cu atom in hexagonal unit cells of 240 ($2 \times 4 \times 1$) atoms. The Cu/Fe ratio corresponds to 1/96, thus mimicking 1% La concentration.

For CH_4 activation barrier calculations, the climbing-image nudged elastic band (CI-NEB) method was used. This method enabled the stationary points to be mapped out along the minimum energy paths and identify transition states for each of the diffusion processes. Because these paths were directed by force projection, the energy was not necessarily consistent with the force being optimized; thus, the force-based optimizer was chosen to ensure the convergence of the nudged elastic band algorithm.
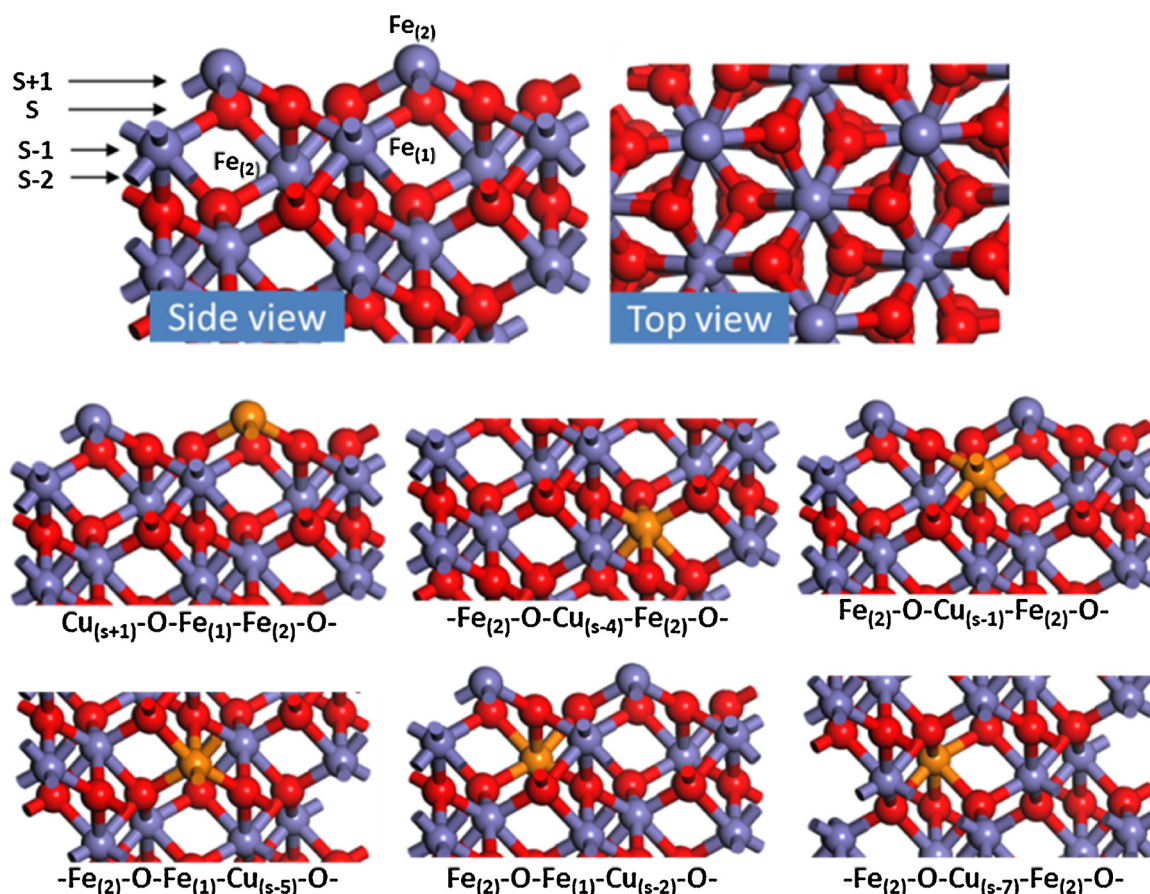
Based on this model and proposed mechanism cycles above, we can map the energy profile of CH_4 oxidation pathways by CI-NEB method. However, the energy barriers need to be corrected using thermo-chemistry model due to chemical looping environment. We previously developed a modified Brønsted–Evans–Polanyi relationship to calculate the activation energy for the elementary steps of metathesis reaction [18]. Here, we extend this method to calculate the energy barriers for CH_4 oxidation at high temperature using the equation below:

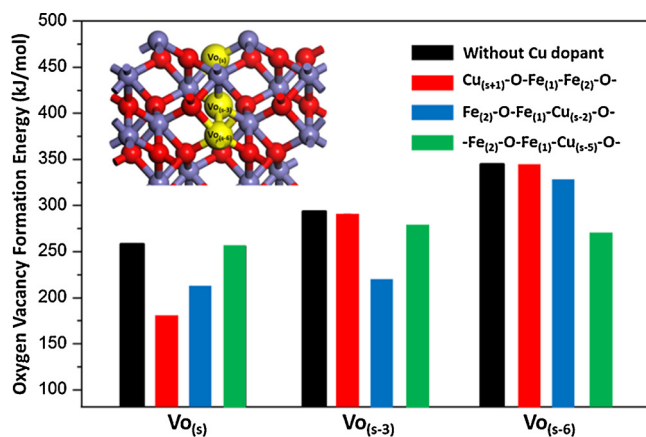$$E_a(T) = E_{a,DFT} + \alpha (\Delta H_r(T) - \Delta E_{r,DFT})$$

where $E_{a,DFT}$ corresponds to the forward activation energy barrier at 0 K, which is obtained from CI-NEB calculations. $\Delta H_r(T)$ is the reaction enthalpy at finite temperature, which is calculated from the individual enthalpies of the initial state and the final state for the constituent elementary reactions. $\Delta E_{r,DFT}$ is the difference between the energies of final state and initial state at 0 K. The variable α denotes the relative position of the transition state compared to the initial (i.e., α = 0) or final (i.e., α = 1) state of the relevant elementary dissociation reaction. It can be obtained by considering which image in the CI-NEB calculations corresponds to the transition state.

To consider this Coulomb repulsion explicitly, we applied DFT + U correction, which consists of combining the DFT with a Hubbard-Hamiltonian term [19,20]. When increasing U from 1 eV to 4 eV, it results in improved values for magnetic moments and band gap as well as better agreement with density of states by experimental IPS spectra. In addition, the band gap becomes too large and occupied Fe 3d states are shifted to too low energies, i.e., U > 4.2 eV. Therefore, we choose

Fig. 5. Fe$_2$O$_3$ slab with Fe(2)-O-Fe(1)-Fe(2)-O- termination. The yellow balls denote oxygen vacancies in the top surface and subsurface, the purple balls denote Fe atoms, the red balls denote oxygen atoms and orange ball denote Cu atom (For interpretation of the references to colour in this figure legend, the reader is referred to the web version of this article).

Fig. 6. Oxygen vacancy formation energies for different oxygen vacancies on Fe$_2$O$_3$ surface with Cu dopant.

U = 4 eV to describe the energy required for adding an extra *d* electron to Fe atom [21].

3. Results and discussion

1% Cu-doped Fe$_2$O$_3$ was synthesized using modified Pechini method. SEM images in Fig. 2a and b indicate that 1% Cu-doped Fe$_2$O$_3$ has similar average grain size compared with the phase pure Fe$_2$O$_3$, which are 4.6 μm and 4.4 μm, respectively. The average grain sizes are identical, i.e. 4.3 μm, after 50 redox cycles in the undoped and doped

oxides. This implies that the Cu-doped Fe$_2$O$_3$ has less morphological change, which is advantageous in CLPO. The impact of 1% Cu dopant on crystal structure modification was studied by XRD. Fig. 2c and d show the XRD patterns of as-prepared rhombohedral Fe$_2$O$_3$ (Fig. 2c (1)) and 1% Cu-doped Fe$_2$O$_3$ (Fig. 2c (3)). No impurity phase was observed in 1% Cu-doped Fe$_2$O$_3$ samples, indicating Cu is completely doped in Fe$_2$O$_3$ in the modification. On the other hand, high resolution XRD spectra suggest a slight red shift of the diffraction peaks in 1% Cu-doped Fe$_2$O$_3$ samples compared to Fe$_2$O$_3$ (Fig. 2d), confirming that the dopant incurs lattice parameter shrinkage from a and c with 5.036 Å and 13.75 Å in Fe$_2$O$_3$ to a and c with 5.035 Å and 13.75 Å in Cu-doped Fe$_2$O$_3$. Chemical surface modification analysis is shown in Fig. 3. The Cu 2p peak region has split spin-orbit components with both Cu 2p3/2 and Cu 2p1/2 having satellite features [22,23]. A red shift of Cu 2p3/2 peaks after dopant modification confirms the modification of copper dopant in iron oxide. The O 1s spectra in undoped iron oxide suggests two species on the sample surface (Fig. 3b): metal-oxygen bond (lattice oxide) at 529.3 eV and hydroxyl groups [24] bond at 532.0 eV, respectively. Different with isovalent dopants such as lanthanum, the surface Cu/O ratio is 0.84% from XPS analysis, indicating Cu atoms do not have a tendency to accumulate at the surface. Nonetheless, the ratio of hydroxyl oxide or defective oxide O species expands from 56.9% to 62.8% (Table 1) in 1% Cu-doped Fe$_2$O$_3$ compared to undoped Fe$_2$O$_3$, which is proved to be helpful for methane activation [25].

Fig. 4a and b show the oxygen carrier conversion rates in 15 typical continuous cycles of methane reduction and oxidation regeneration of 1% Cu-doped Fe$_2$O$_3$ and undoped Fe$_2$O$_3$ at 700 °C that is lower than conventional operation temperature. The reduction was carried out in 25% methane balanced by inert gas and the regeneration was

conducted in 25% air balanced by inert gas. All the experiments have been repeated for multiple times and the error bars confirm the high reproducibility of the results. The increase of methane conversion rates is identical in samples of 0.015–0.1 g. The TGA analysis shows that 1% Cu-doped Fe_2O_3 has dramatically increase the conversion rates in methane conversion and oxygen carriers regeneration compared to undoped Fe_2O_3. At 700 °C, the average reduction conversion and regeneration rates of 1% Cu-doped Fe_2O_3 is 474% and 485% higher than that of undoped Fe_2O_3, respectively, as shown in Fig. 4a and b. The high recyclability of the oxygen carriers is also revealed from Fig. 4a and b. This observation is consistent with the less changing morphology evolution.

Additionally, we studied the reactivity enhancement of Cu modification in a wide range of operating temperatures. As shown in Fig. 4c and d, the reactivity of both methane conversion and oxidation regeneration universally increases between 700 °C and 1000 °C. The methane conversion rates of 1% Cu-doped Fe_2O_3 are 474%, 409%, 14% and 15% higher than that of undoped Fe_2O_3 at 700 °C, 800 °C, 900 °C and 1000 °C respectively. The reactivity enhancement is substantial at lower temperature, e.g., 700–800 °C. A high CO selectivity of 90% can be achieved at 800 °C using moving bed reactors [26]. The less significant conversion rate increase is likely associated with dopant-induced high temperature sintering effect.

To gain the insight into the role of 1% Cu doping in the reactivity of Fe_2O_3, we model the 1% Cu-Fe_2O_3 slab and examine CH_4 activation in this slab system. Recently, Wang et al. employed the DFT + U method to study the water interaction with α-Fe_2O_3 and revealed that its surface termination can significantly affect gas molecule adsorption [27]. Therefore, we first determined the stable iron oxide surface termination state, assuming Fe_2O_3 cleaving along the (001) surface, which was proven to be the dominant surface in the X-ray photoelectron diffraction study [28]. A 15 Å-thick vacuum layer was used to separate the surfaces and their images. The use of periodic models eliminates edge effects and allows for a more accurate description of surface relaxation. Depending on the cleavage position and the repeat of iron and oxygen atoms ordering, three possible terminations can be built: O-$Fe_{(1)}$-$Fe_{(2)}$-O-$Fe_{(1)}$- and $Fe_{(2)}$-O-$Fe_{(1)}$-$Fe_{(2)}$-O- and $Fe_{(1)}$-$Fe_{(2)}$-O-$Fe_{(1)}$-$Fe_{(2)}$-.

Based on surface free energy calculation for Fe_2O_3 (001) surface with these terminations, we found $Fe_{(2)}$-O-$Fe_{(1)}$-$Fe_{(2)}$-O- termination is the most stable [29]. Therefore, substitutions were made at the slab with $Fe_{(2)}$-O-$Fe_{(1)}$-$Fe_{(2)}$-O- termination. Using the first oxygen layer as the reference layer s, we replaced Fe(2) at the s + 1 layer with one Cu atom to build the doping system $Cu_{(s + 1)}$-O-$Fe_{(1)}$-$Fe_{(2)}$-O-. Then we used one Cu atom to replace $Fe_{(1)}$ at the s-1 layer to build $Fe_{(2)}$-O-$Cu_{(s-1)}$-$Fe_{(2)}$-O- system, or $Fe_{(2)}$ at the s-2 layer to build $Fe_{(2)}$-O-$Fe_{(1)}$-$Cu_{(s-2)}$-O- system as shown in Fig. 5. It was found that the surface free energy of $Cu_{(s + 1)}$-O-$Fe_{(1)}$-$Fe_{(2)}$-O- system is 1.35 J/m^2, while the surface free energy of Fe(2)-O-$Cu_{(s-1)}$-$Fe_{(2)}$-O- and $Fe_{(2)}$-O-$Fe_{(1)}$-$Cu_{(s-2)}$-O- system is 1.33 J/m^2 and 1.38 J/m^2, respectively. Similarly, we replaced Fe atom in s-4. s-5, s-7 layer, and found the surface free energy of -$Fe_{(2)}$-O-$Cu_{(s-4)}$-$Fe_{(2)}$-O-, -$Fe_{(2)}$-O-$Fe_{(1)}$-$Cu_{(s-5)}$-O- and -$Fe_{(2)}$-O-$Cu_{(s-7)}$-$Fe_{(2)}$-O-system is 1.34 J/m^2, 1.35 J/m^2 and 1.33 J/m^2, respectively. It indicates that the substitution may occur on the surface or subsurface, which agrees with the experimental finding that Cu dopant atoms do not have a tendency to accumulate at the surface.

In CH_4 activation process, adsorbed CH_x radicals on the surface accepts oxygen atoms from the iron oxide which leads to oxygen vacancy formation. To study the oxygen vacancy formation, the $Fe_{(2)}$-O-$Cu_{(s-1)}$-$Fe_{(2)}$-O- terminated surface was used since it is the most favorable α-Fe_2O_3 (001) surface at 700 °C. α-Fe_2O_3 (001) surface has the stoichiometric (Fe–Fe–O3) sequence in the slab geometry with a lateral periodicity represented by a hexagonal crystal lattice. We removed one lattice oxygen atom in the first O3 layer (s layer) to create an oxygen vacancy on the top surface $Vo_{(s)}$. Similarly, we removed one lattice oxygen atom in the second O3 layer (s-3 layer) and in the third O3 layer (s-6 layer) to create the oxygen vacancy $Vo_{(s-3)}$ and $Vo_{(s-6)}$, respectively.

The calculated oxygen vacancy formation energies for Fe_2O_3 (001) surface with Cu dopant are shown in Fig. 6. For pristine Fe_2O_3 surface, $Vo_{(s)}$ is the most energetically favorable oxygen vacancy with vacancy formation energy of 258.56 kJ/mol, while the vacancy formation energies for $Vo_{(s-3)}$ and $Vo_{(s-6)}$ are 292.51 kJ/mol and 342.43 kJ/mol, respectively. Therefore, the oxygen vacancy on the top surface of Fe_2O_3 is easier to form than the vacancy in the subsurface. In addition, it can be seen that Cu dopant decreases the formation energy of $Vo_{(s)}$. For $Cu_{(s + 1)}$-O-$Fe_{(1)}$-$Fe_{(2)}$-O- system, the vacancy formation energy of Vo(s) is 178.08 kJ/mol, which is 80.48 kJ/mol lower than that on Fe_2O_3 surface without Cu dopant. However, for $Fe_{(2)}$-O-$Fe_{(1)}$-$Cu_{(s-2)}$-O- system, the vacancy formation energy of Vo(s) is 211.73 kJ/mol which is only 46.83 kJ/mol lower than that on Fe_2O_3 surface without Cu dopant, It indicated that the closer the dopant is to the oxygen vacancy, the stronger the interaction is. For the subsurface oxygen vacancy $Vo_{(s-3)}$ and $Vo_{(s-6)}$, Cu doping also results in a decrease of the oxygen vacancy formation energy when Cu dopant is close to the oxygen vacancy. Therefore, Cu doping can significantly facilitate oxygen vacancy formation on the surface and subsurface. We further investigated CH_4 activation on Cu doped Fe_2O_3 surface with oxygen vacancies.

We have found oxygen vacancies play an essential role on CH_4 partial oxidation on Fe_2O_3 surface [30]. Here we further investigate the effect of oxygen vacancy $Vo_{(s)}$, $Vo_{(s-3)}$ and $Vo_{(s-6)}$ on CH_4 activation on Cu doped Fe_2O_3 surface. Upon the first step of CH_4 dissociation on the Cu site with a neigboring surface oxygen vacancy Vo(s), the formed CH_3 radical may react with Fe_2O_3 via O-H path where CH_3 remains on the Cu site while H atom migrates to the surface oxygen site, or via Cu-H path where the CH_3 radical is adsorbed to the neighboring oxygen vacancy site, whereas H remains on the original Cu adsorption site. The calculation shows that Cu-H path is more favorable with a barrier of 73.32 kJ/mol, which is 92.63 kJ/mol lower than energy barrier on pristine Fe_2O_3 surface. For Cu doped Fe_2O_3 surface with $Vo_{(s-3)}$ vacancy and Cu doped Fe_2O_3 surface with Vo(s-6) vacancy, the calculated CH_4 activation barriers are 103.58 kJ/mol and 146.89 kJ/mol, respectively. Therefore, we conclude that the 1% Cu dopant does significantly lower the energy barrier of CH_4 activation on Fe_2O_3, compared to the control case of undoped iron oxide. Actually, the activity is determined by a series of oxidation state while gradually reduced in the chemical looping combustion process. We also examine 1% Cu dopant effect on Fe_3O_4 and FeO reactivity. 1% Cu-Fe_3O_4 has a cubic inverse spinel structure with a lattice constant of 8.391 Å (8.396 Å for Fe_3O_4). The O anions form a close-packed face-centered cubic (fcc) structure with Fe^{2+} and Fe^{3+} ions located in the interstitial sites. Based on this model, we calculate the CH_4 activation barrier and found it is 81.3 kJ/mol lower than that on undoped Fe_3O_4. Also, the barrier of CH_4 activation on 1%Cu-FeO is 78.1 kJ/mol lower than that on the undoped surface. Our results confirm that Cu dopants can significantly enhance the catalytic activity of iron oxide for CH_4 conversion, which has been observed by the TGA experiments.

4. Conclusions

In summary, Cu dopant with low concentration in Fe_2O_3 oxygen carriers can dramatically facilitate CH_4 conversion as well as iron-based oxygen carrier regeneration activity while maintaining their recyclability. It is found that the reactivity of Cu-doped oxygen carriers is higher than that of undoped iron oxide oxygen carriers universally between 700 °C and 1000 °C. The maximum reactivity increase happens at 700 °C where the CH_4 conversion rate increases by 474% and the air regeneration reactivity increased by 485%. For a typical chemical looping partial oxidation system, the decrease in operating temperature from 1000 °C to 700 °C can result in energy consumption savings of ~35%. The mechanism for the reactivity enhancement of Cu dopant-based oxygen carrier stems from the ability of Cu dopants in facilitating the formation the oxygen vacancies in Fe_2O_3 oxygen carriers, which significantly lowers the barrier of CH_4 activation during the redox

reaction. Our findings yield a pathway to dramatic metal oxide oxygen carrier property modification using a relatively simple fabrication process, which will have an impact on future chemical looping particle design.

Author contributions

The manuscript was written through contributions of all authors. All authors have given approval to the final version of the manuscript.

Acknowledgements

References

[1] L.-S. Fan, Chemical Looping Partial Oxidation: Gasification, Reforming, and Chemical Syntheses, Cambridge University Press, 2017.

[2] M. Fathi, E. Bjorgum, T. Viig, O. Rokstad, Partial oxidation of methane to synthesis gas:: elimination of gas phase oxygen, Catal.Today 63 (2000) 489–497.

[3] P. Pantu, K. Kim, G.R. Gavalas, Methane partial oxidation on Pt/CeO_2–ZrO_2 in the absence of gaseous oxygen, Appl. Catal. A: Gen. 193 (2000) 203–214.

[4] F. He, Y. Wei, H. Li, H. Wang, Synthesis gas generation by chemical-looping reforming using Ce-based oxygen carriers modified with Fe, Cu, and Mn oxides, Energy Fuels 23 (2009) 2095–2102.

[5] K.-z. Li, H. Wang, Y.-g. Wei, M.-c. Liu, Partial oxidation of methane to syngas using lattice oxygen from ceria-based complex oxides oxygen carriers, J. Fuel Chem. Technol. 36 (2008) 83.

[6] W. Yonggang, W. Hua, L. Kongzhai, Z. Xing, D. Yunpeng, Preparation and characterization of $Ce_{1-x}Ni_xO_2$ as oxygen carrier for selective oxidation methane to syngas in absence of gaseous oxygen, J. Rare Earths 28 (2010) 357–361.

[7] A. Yaremchenko, V. Kharton, S. Veniaminov, V. Belyaev, V. Sobyanin, F. Marques, Methane oxidation by lattice oxygen of $CeNbO_{4+\delta}$, Catal. Commun. 8 (2007) 335–339.

[8] R.-J. Li, C.-C. Yu, W.-J. Ji, S.-K. Shen, Methane oxidation to synthesis gas using lattice oxygen in $La_{1-x}Sr_xFeO_3$ perovskite oxides instead of molecular oxygen, Stud. Surf. Sci. Catal. 147 (2004) 199–204.

[9] R. Li, C. Yu, X. Dai, S. Shen, Selective oxidation of methane to synthesis gas using lattice oxygen from perovskite $La0.8Sr_{0.2}FeO_3$ catalyst, Chin. J. Catal. 23 (2002) 549–554.

[10] M. Rydén, A. Lyngfelt, T. Mattisson, D. Chen, A. Holmen, E. Bjørgum, Novel oxygen-carrier materials for chemical-looping combustion and chemical-looping reforming; $La_xSr_{1-x}Fe_yCo_{1-y}O_{3-\delta}$ perovskites and mixed-metal oxides of NiO, Fe2O3 and Mn_3O_4, Int. J. Greenhouse Gas Control 2 (2008) 21–36.

[11] C. Chung, L. Qin, V. Shah, L.-S. Fan, Chemically and physically robust, commercially-viable iron-based composite oxygen carriers sustainable over 3000 redox cycles at high temperatures for chemical looping applications, Energy Environ. Sci. 10 (2017) 2318–2323.

[12] L. Qin, Z. Cheng, M. Guo, M. Xu, J.A. Fan, L.-S. Fan, Impact of 1% lanthanum dopant on carbonaceous fuel redox reactions with an iron-based oxygen carrier in chemical looping processes, ACS Energy Lett. 2 (2016) 70–74.

[13] L. Qin, M. Guo, Z. Cheng, M. Xu, Y. Liu, D. Xu, J.A. Fan, L.-S. Fan, Improved cyclic redox reactivity of lanthanum modified iron-based oxygen carriers in carbon monoxide chemical looping combustion, J. Mater. Chem. A 5 (2017) 20153–20160.

[14] G. Kresse, J. Furthmüller, Efficiency of ab-initio total energy calculations for metals and semiconductors using a plane-wave basis set, Comput. Mater. Sci. 6 (1996) 15–50.

[15] G. Kresse, J. Furthmüller, Efficient iterative schemes for ab initio total-energy calculations using a plane-wave basis set, Phys. Rev. B 54 (1996) 11169.

[16] G. Kresse, J. Hafner, Ab initio molecular dynamics for liquid metals, Phys. Rev. B 47 (1993) 558.

[17] J.P. Perdew, K. Burke, M. Ernzerhof, Generalized gradient approximation made simple, Phys. Rev. Lett. 77 (1996) 3865.

[18] Z. Cheng, C.S. Lo, Propagation of olefin metathesis to propene on WO_3 catalysts: a mechanistic and kinetic study, ACS Catal. 5 (2014) 59–72.

[19] J. Herbst, R. Watson, J. Wilkins, Relativistic calculations of 4 f excitation energies in the rare-earth metals: further results, Phys. Rev. B 17 (1978) 3089.

[20] V. Anisimov, O. Gunnarsson, Density-functional calculation of effective Coulomb interactions in metals, Phys. Rev. B 43 (1991) 7570.

[21] G. Rollmann, A. Rohrbach, P. Entel, J. Hafner, First-principles calculation of the structure and magnetic phases of hematite, Phys. Rev. B 69 (2004) 165107.

[22] S. Poulston, P. Parlett, P. Stone, M. Bowker, Surface oxidation and reduction of CuO and Cu_2O studied using XPS and XAES, Surf. Interface Anal. 24 (1996) 811–820.

[23] M.C. Biesinger, L.W. Lau, A.R. Gerson, R.S.C. Smart, Resolving surface chemical states in XPS analysis of first row transition metals, oxides and hydroxides: Sc, Ti, V, Cu and Zn, Appl. Surf. Sci. 257 (2010) 887–898.

[24] M.C. Biesinger, B.P. Payne, L.W. Lau, A. Gerson, R.S.C. Smart, X-ray photoelectron spectroscopic chemical state quantification of mixed nickel metal, oxide and hydroxide systems, Surf. Interface Anal. 41 (2009) 324–332.

[25] X. Tang, J. Hao, J. Li, Complete oxidation of methane on Co3O4-SnO2 catalysts, Front. Environ. Sci. Eng. China 3 (2009) 265–270.

[26] S. Luo, L. Zeng, D. Xu, M. Kathe, E. Chung, N. Deshpande, L. Qin, A. Majumder, T.-L. Hsieh, A. Tong, Shale gas-to-syngas chemical looping process for stable shale gas conversion to high purity syngas with a H_2: CO ratio of 2: 1, Energy Environ. Sci. 7 (2014) 4104–4117.

[27] R.B. Wang, A. Hellman, Initial water adsorption on hematite (α-Fe2O3)(0001): a DFT++ U study, J. Chem. Phys. 148 (2018) 094705.

[28] R.L. Kurtz, V.E. Henrich, Geometric structure of the α-Fe2O3 (001) surface: a LEED and XPS study, Surf. Sci. 129 (1983) 345–354.

[29] Z. Cheng, L. Qin, M. Guo, M. Xu, J.A. Fan, L.-S. Fan, Oxygen vacancy promoted methane partial oxidation over iron oxide oxygen carriers in the chemical looping process, Phys. Chem. Chem. Phys. 18 (2016) 32418–32428.

[30] Z. Cheng, L. Qin, M. Guo, J.A. Fan, D. Xu, L.-S. Fan, Methane adsorption and dissociation on iron oxide oxygen carriers: the role of oxygen vacancies, Phys. Chem. Chem. Phys. 18 (2016) 16423–16435.